

# Characterizing the nuclease accessibility of DNA in human cells to map higher order structures of chromatin

Uwe Schwartz<sup>1</sup>, Attila Németh<sup>1</sup>, Sarah Diermeier<sup>1</sup>, Josef H. Exler<sup>1</sup>, Stefan Hansch<sup>1</sup>, Rodrigo Maldonado<sup>1</sup>, Leonhard Heizinger<sup>2</sup>, Rainer Merkl<sup>2</sup> and Gernot Längst<sup>1,\*</sup>

<sup>1</sup>Department of Biochemistry III, University of Regensburg, University of Regensburg, 93040 Regensburg, Germany and <sup>2</sup>Institute of Biophysics and Physical Biochemistry, University of Regensburg, 93040 Regensburg, Germany

Received October 10, 2018; Revised November 17, 2018; Editorial Decision November 19, 2018; Accepted November 22, 2018

## ABSTRACT

**Packaging of DNA into chromatin regulates DNA accessibility and consequently all DNA-dependent processes. The nucleosome is the basic packaging unit of DNA forming arrays that are suggested, by biochemical studies, to fold hierarchically into ordered higher-order structures of chromatin. This organization has been recently questioned using microscopy techniques, proposing an irregular structure. To address the principles of chromatin organization, we applied an *in situ* differential MNase-seq strategy and analyzed *in silico* the results of complete and partial digestions of human chromatin. We investigated whether different levels of chromatin packaging exist in the cell. We assessed the accessibility of chromatin within distinct domains of kb to Mb genomic regions, performed statistical analyses and computer modelling. We found no difference in MNase accessibility, suggesting no difference in fiber folding between domains of euchromatin and heterochromatin or between other sequence and epigenomic features of chromatin. Thus, our data suggests the absence of differentially organized domains of higher-order structures of chromatin. Moreover, we identified only local structural changes, with individual hyper-accessible nucleosomes surrounding regulatory elements, such as enhancers and transcription start sites. The regulatory sites per se are occupied with structurally altered nucleosomes, exhibiting increased MNase sensitivity. Our findings provide biochemical evidence that supports an irregular model of large-scale chromatin organization.**

## INTRODUCTION

The sequence-specific binding of proteins to DNA determines the activity of DNA-dependent processes, such as transcription, replication, repair and others, regulating cellular fate. However, nuclear DNA is packaged into chromatin, a nucleoprotein structure that restricts the access of specific DNA binding proteins. As a first level of compaction, DNA segments of 147 bp are wrapped in 1.7 left-handed turns around histone octamers forming the nucleosome core, each having a diameter of 11 nm. Thus, the human genome is covered by ~30 million nucleosome cores, which are separated by DNA linkers whose length is cell-type specific and ranges between 20 and 75 bp (1–3). Nucleosomal arrays are the building blocks for higher levels of compaction and are assumed to fold at an intermediate level into fibres of 30, 120, 300 and 700 nm in diameter, which ultimately constitute the mitotic chromosome (3). This textbook model of hierarchical folding is based on the analysis of *in vitro* reconstituted chromatin and on chromatin extracted from permeabilized cells. The latest *in vitro* studies propose two alternative models for the 30 nm fibre: the one-start solenoid (4) and the two-start zig-zag with approximately five to six nucleosomes per 11 nm of fibre (5,6).

The existence of the 30 nm fibre and additional levels of chromatin folding *in vivo* remains a controversial topic. Contrary to the textbook model, organized structures have been observed in terminally differentiated cells and specialized cells such as starfish sperm but not in proliferating cells (7–10). Additionally, a further series of experiments suggests that nucleosomes are highly interdigitated and do not form regular 30 nm fibres but irregular folded structures. These findings are best described by a polymer melt model (11–17). However, alternative higher-order structures, being incompatible with the polymer melt model, have been described for metaphase and interphase chro-

\*To whom correspondence should be addressed. Tel: +49 941943 2849; Email: gernot.laengst@vkl.uni-regensburg.de  
Present addresses:

Attila Németh, Institute of Neuropathology, Justus Liebig University, Aulweg 128, 35392 Giessen, Germany.

Sarah Diermeier, Department of Biochemistry, University of Otago, 710 Cumberland Street, Dunedin 9016, New Zealand.

mosomes. Among them is the ‘rope flaking’ model, having the nucleosomal arrays looped without self-crossing (18). Such an organization would explain the release of several hundred kb-long chromatin loops after gentle lysis of the metaphase chromosomes (19). This model is supported by electron microscopic analysis, nuclease and topoisomerase II accessibility assays, suggesting that higher-order structures of chromatin are organized into 50 kb domains that form more compacted structures of 300 kb (20,21). Taken together, these findings indicate that chromatin organization is still an enigma.

The degree of chromatin folding into higher order structures is also correlated with gene transcription and is thought to impact the regulation of DNA-dependent processes. In paradigmatic studies, the sedimentation of the  $\beta$ -globin gene was monitored in sucrose gradients. Compared to bulk chromatin, a slower sedimentation was observed for the active gene, suggesting open chromatin (20,21). Indeed, gene-rich domains are generally de-compacted chromatin regions that are maintained by the actively transcribing RNA polymerases and the altered degree of DNA supercoiling (22,23). Still, there is microscopic evidence that actively transcribed genes exist in a chromatin structure that is approximately 25 times more compact than the nucleosomal array, and only a 1.5- to 3-fold extension of the compacted fibre is observed upon transcriptional activation (24). Whether these changes in chromatin compaction are associated with a change of chromatin density or a loss of hierarchical packaging is not known.

High-throughput sequencing technologies allow the precise mapping of nucleosome positions throughout the genome and can reveal dynamic changes of nucleosome positions depending on the cell types or activating signals (25–29). Recent studies have demonstrated disease-dependent differences in nucleosome positions in tissues and cell lines, suggesting an important role of chromatin architecture on cell fate (30). However, these methods fail to elucidate the higher-order structures of chromatin. A recent study combined the Micro-C method with chromatin fragmentation by micrococcal nuclease (MNase) in budding yeast (15). This approach allowed for chromatin analysis in the range of 200 bp–4 kb, which would be suitable to address the organization of the 30 nm fibres. But this study did not analyze global chromatin organization and suggested a variety of local folding motifs. Chromatin fragmentation using varying concentrations of MNase was used to reveal local changes in chromatin accessibility, and not focusing on the organization of higher order structures of chromatin (31–33).

We devised a strategy to analyze differential chromatin accessibility from nucleosome resolution up to 1 Mb-size domains by comparing partial (low concentration) and complete (high concentration) MNase digestions of chromatin *in situ*. We generated high-coverage chromatin accessibility maps for HeLa cells and identified differential enrichment of high and low MNase-associated DNA fragments on large domains. Our systematic analysis revealed that coverage variations in the datasets show only sequence modulations, and therefore suggesting the absence of distinct higher-order structures of chromatin in cells. Surprisingly, transcriptionally active domains have similar DNA

accessibilities as heterochromatin domains and respectively like all other larger epigenomically defined domains. Furthermore, we identified only local distortions of the MNase accessibility, representing hyper-accessible sites coinciding with active regulatory elements. Hyper-accessible sites are associated with individual MNase-sensitive nucleosomes, which are lost in high MNase but maintained in low MNase digestions. Thus, this analysis gives new insights into chromatin organization, suggesting that no global differences in DNA packaging do exist, challenging the model of hierarchically organized higher-order structures of chromatin.

## MATERIALS AND METHODS

### Differential MNase hydrolysis and DNA isolation

Human adenocarcinoma cells of the HeLa line were cultured in D-MEM medium supplemented with 10% FCS. Cells were incubated at 37°C with 5% CO<sub>2</sub> on 15 cm cell culture dishes. Cells were grown to 70–80% confluence and dishes were washed once with 5 ml PBS. Cells were incubated for 90 s with 3 ml of permeabilisation buffer (15 mM Tris–HCl pH 7.6, 300 mM saccharose, 60 mM KCl, 15 mM NaCl, 4 mM CaCl<sub>2</sub>, 0.5 mM EGTA, 0.2% (v/v) NP40 and fresh 0.5 mM 2-mercaptoethanol) including 100–2000 units of MNase (Sigma) (34). The DNA hydrolysis reaction was stopped by the addition of 3 ml of stop buffer (50 mM Tris–HCl pH 8, 20 mM EDTA and 1% SDS). RNA was digested by the addition of 250  $\mu$ g RNase A and incubation for 2 h. Subsequently 250  $\mu$ g of proteinase K were added to the culture dishes and incubated overnight at 37°C. Fragmented DNA was purified by ammonium acetate and ethanol precipitation. The MNase digestion pattern was analyzed on 1.3% agarose gels and visualized after ethidium bromide staining.

MNase digestion reactions were loaded on preparative agarose gels (1.1% agarose) electrophoresed and the mono-, di- and tri-nucleosomal DNA were excised after ethidium bromide staining. DNA was purified by electroelution using the Electro-Eluter 422 (BioRad). DNA was precipitated and re-analyzed by agarose gel electrophoresis.

### 2D and 3D fluorescence *in situ* hybridisation

The isolated tri-nucleosomal DNA isolated from low- and high-MNase samples were labelled with the Prime-it Fluor Fluorescence Labelling Kit (Stratagene) according to manufacturers’ protocol. 1  $\mu$ g of total DNA was labelled with fluor-12-dUTP or Cy3-dUTP using the random priming protocol.

2D FISH experiments were performed on metaphase spreads of normal human lymphocytes, as described (35). Cot1 DNA (10  $\mu$ g) was used in the hybridisation reactions to suppress the signals of repetitive DNA regions.

3D FISH experiments were performed as described (35). IMR90 human diploid fibroblast cells were fixed and 3D FISH experiments were performed. Confocal microscopy and image analysis were done after 3D FISH experiments as follows: A series of optical sections through 3D-preserved nuclei were collected using a Leica TCS SP5 confocal system equipped with a Plan Apo 63-/1.4 NA oil immersion objective and a diode laser (excitation wave length 405 nm)

for DAPI, a DPSS laser (561 nm) for Cy3 and a HeNe laser (633 nm) for Cy5. For each optical section, signals in different channels were collected sequentially. Stacks of 8-bit grey-scale images were obtained with z-step of 200 nm and pixel sizes 30 - 100 nm depending on experiment.

### DNA sequencing, alignment and data processing

Sequencing libraries of the high and low MNase treated nucleosomal DNA (mono- and di-nucleosomal DNA) were prepared using the NEBNext DNA Library Prep Master Kit (New England Biolabs, Ipswich, USA) and paired-end ( $2 \times 50$  bp) sequenced on a HiSeq2000 platform (Genecore, EMBL, Heidelberg). The sequenced paired-end reads were mapped to the UCSC human genome version 37 (hg19) using the local alignment option of bowtie2 with following parameters—`very-sensitive-local` and—`no-discordant` (36). Aligned reads were filtered for mapping quality ( $\text{MAPQ} > 20$ ) and further processed using SAMtools (37) and BEDtools (38). Fragments with a size of 140–200 bp were considered to originate from mono-nucleosomal protected DNA and fragments with a size of 250–500 bp as di-nucleosomal respectively. All downstream analyses were performed on the filtered and size-selected fragments.

### Genome wide nucleosome maps

Genome wide nucleosome occupancy maps were generated using the `danpos.py` script from the DANPOS2 toolkit (39) in `dpos` mode. Here, reads were extended to 70 bp following the centering to the fragment midpoint, to obtain focused mono-nucleosomes (150 bp for di-nucleosomes). Clonal reads were filtered using the parameter `u 1E-2` and the total number of fragments was normalized to 200 million fragments for each sample.

Obtained nucleosome occupancy maps were further processed using Control-FREEC v8.7 to call copy number alterations (CNV) in HeLa cells (40). Control-FREEC was ran on single-end high-throughput sequencing data of sonicated chromatin in HeLa cells, which were annotated as above, except that reads were not filtered without matching read-pair as unbiased control with following settings: `ploidy = 3`, `window = 500 000`, `step = 50 000`, `minMappabilityPerWindow = 0.80`, `breakPointThreshold = 3`. The algorithm also accounts for the underlying GC content and mappability of the genome. Therefore, the provided mappability track covering up to two mismatches for 50 bp single-end reads (available at <http://boevalab.com/FREEC/>) and a GC profile consisting of 500 kb sliding windows with 50 kb steps have been integrated in the analysis. Finally, nucleosome occupancy maps have been normalized by the reported CNVs.

### Differential MNase analysis

The complete human genome (hg19) was segmented in non-overlapping windows of a constant size (ranging from 250 bp to 1 Mb). The average nucleosome profile level of each MNase condition, the average GC content and mappability score which was based on CRG alignability track for

100mers (41), was calculated for each window. Windows lacking mapped reads or exhibiting an average mappability score below 0.9, were excluded from further analyses. Linear regression analysis was carried out in the R environment (42) applying the implemented linear regression function (`lm`). Extreme values exhibiting a high influence on the regression analysis were filtered using a Cook's distance threshold of 0.001. Adjusted  $R^2$  values reported by `lm` were used to assess the dependency of the tested features. Density plots were drawn with the `heatscatter` function implemented in the R package LSD (43).

### GC content and di-nucleotide frequency of nucleosomal fragments

The average GC content and dinucleotide frequency around the borders of mapped fragments were calculated using the `makeTagDirectory` script from the HOMER software package (44). To calculate the dinucleotide frequency around the midpoints of mapped fragments, properly aligned read-pairs were converted to a bed format comprising start and end positions of the fragments using BEDtools. The dinucleotide frequency was obtained by applying the `annotatePeaks.pl` script of the HOMER software package with the parameters `-hist 1, --di --size -300,300`.

### Nucleosome prediction, average nucleosome occupancy profiles and heatmaps

The `dpos` script from the DANPOS2 toolkit was applied to the normalized nucleosome occupancy profiles with default settings in order to predict nucleosome positions (39). Average nucleosome occupancy profiles and/or heatmaps around factor binding sites, transcription start sites or DNase I HS were generated using the DANPOS2 script `profile`.

### GC normalization and detection of local differential chromatin accessibility

A locally weighted scatterplot smoothing (LOESS) was applied to correct for the inherent GC bias in the nucleosome occupancy profiles. Therefore, the average nucleosome profile level and GC content within 250 bp non-overlapping windows were calculated and filtered as described above. Additionally, windows exhibiting an extreme GC content ( $<30\%$  or  $>70\%$ ) were filtered. The `loess` function implemented in the R environment was applied to estimate the influence of GC content on high or low MNase digestions. The nucleosome occupancy profile in the 250 bp windows was corrected by the LOESS analysis determined correction factor. Local differences of GC-normalized low and high MNase nucleosome occupancy profiles were determined using the `dpeak` algorithm of the DANPOS2 toolkit with the parameters `--peak.width 70, --p 1E-2`. Differentially enriched peaks were selected by a false discovery rate (FDR)  $<0.05$  and were termed as MNase hyper-accessible (enriched in low MNase) or MNase in-accessible (enriched in high MNase).

## Simulation of MNase digestions

Simulations were conducted on an artificially generated nucleosome fibre comprising of 50 nucleosomes of 150 bp in size, regularly spaced onto a 9000 bp long DNA strand. One potential MNase cleavage site was assigned to each linker DNA and each nucleosome. First, an index containing the positions of the potential cleavage sites  $PosCut$  was created. Cleavage sites  $posCut_i$  were assigned to every 90 bp ((150 bp nucleosomal DNA + 30 bp linker DNA)/2) of the 9000 bp long strand, representing alternating linker  $posCut(linker)_i$  and nucleosome  $posCut(nuc)_i$  cleavage sites. Every second  $posCut(nuc)$  was shifted 5 bp downstream, consequently  $posCut(nuc)_{i+1} - posCut(nuc)_i = 180 \pm 5$  bp and  $posCut(linker)_{i+1} - posCut(linker)_i = 180$  bp.

In total, this generated an index of the cleavage positions along the simulated DNA strand:

$$\begin{aligned} PosCut &= (posCut(linker)_1 = 0, posCut(nuc)_1 \\ &= 85, posCut(linker)_2 \\ &= 180, posCut(nuc)_2 = 270, \dots, posCut(nuc)_{50} \\ &= 8910, posCut(linker)_{51} = 9000). \end{aligned}$$

In the next step, the  $posCut(nuc)_i$  and  $posCut(linker)_i$  values were sampled according to their associated probability of an intra-nucleosomal MNase cleavage event, namely  $p_{cut}(nuc)$  or inter-nucleosomal MNase cleavage event  $p_{cut}(linker)$ . Initially, we chose the probability of  $p_{cut}(linker) = 10 \cdot p_{cut}(nuc)$  according to *in vitro* studies (45). Subsequent values were adapted as indicated in the text. From this distribution,  $n$  values  $posCut(nuc)_i$  or  $posCut(linker)_i$  were randomly drawn without replacement, simulating  $n$  cutting events on one template. For high MNase simulations,  $n = 70$  cutting events were chosen per template and  $n = 20$  for low MNase simulations. The corresponding cutting positions  $posCol$  were sorted in ascending order:  $PosCol = (posCol_1 < posCol_2 < \dots < posCol_n)$ .

Neighbouring positions  $posCol_j$  were assembled into fragments  $fr(posCol_i, posCol_{i+1})$  and fragments of 180 bp length were stored, since they represent the simulated mono-nucleosomes. This process was iterated until one million fragments of 180 bp length were sampled. Finally, the nucleosomal fragments were trimmed by 30 bp from both sides to centre the nucleosome positions and the coverage over the simulated strand was plotted.

## External data sets used in this study

DNase-seq (ENCSR959ZXU), CTCF binding sites (ENCSR000CUB), H3K27ac-ChIP (ENCF311EWS), H3K27me3-ChIP (ENCF958BAN), and polyA mRNA RNA-seq (ENCSR000EYQ) tracks were downloaded from the ENCODE repository (46,47). Chromatin state annotation for HeLa cells (E115, 15 core marks) was obtained from the roadmap epigenomics project (48). Enhancer site analysis was carried out using the predefined HeLa enhancer sets from (49). CRG mappability (align 100 mer) track was downloaded from the UCSC browser (<http://hgdownload.soe.ucsc.edu/goldenPath/hg19/encodeDCC/wgEncodeMapability/>).

## RESULTS

### The rationale of the differential MNase-seq strategy

If chromatin forms distinct levels of higher-order structures, with increasing folding from the open and active state to the repressed and inactive state, it follows that DNA accessibility would decrease with increasing self-organisation. As a consequence, we expect that DNA hydrolysis would first release accessible chromatin domains, followed by the release of folded chromatin domains at higher endonuclease concentrations. We used micrococcal nuclease (MNase), an endonuclease that preferentially hydrolyses DNA in the linker region between nucleosomes (50) as a tool to map chromatin accessibility. The feasibility of this approach is suggested as *in vitro* reconstituted and isolated 30 nm fibers from chicken erythrocytes reveal a reduced MNase accessibility, as compared to the unfolded nucleosomal arrays (51).

HeLa cells were permeabilized and incubated with increasing concentrations of MNase for 90 s. The DNA was purified and analyzed on agarose gels, showing increasing fragmentation of chromatin with higher MNase concentrations (Figure 1A). Even though the majority of genomic DNA was not hydrolysed, our lowest MNase concentration gave rise to a nucleosome ladder and also mono-nucleosomal DNA. These findings suggest that the genome is differentially packaged, with domains of either high or low MNase accessibility. This behaviour is expected if distinct levels of chromatin packaging existed in the cell. Thus, we propose that at low-MNase conditions nucleosomes from open and accessible chromatin structures are released preferentially, whereas inaccessible or potentially folded chromatin structures - which are more resistant - are only released at high-MNase conditions.

### An *in silico* model for the differential MNase-seq strategy

To assess our initial assumption, we designed an *in silico* model that allowed us to simulate the effect of differential MNase hydrolysis on a nucleosomal array of 50 nucleosomes (Figure 1B). We chose a stochastic approach and assigned different probabilities  $p_{cut}(\cdot)$  for MNase cleavage of DNA to different regions of the DNA (Supplementary Figure S1A). To begin, we defined two different regions and assigned two different probabilities  $p_{cut}(linker)$  to DNA linker regions and  $p_{cut}(nuc)$  to DNA covered by nucleosomes. The values  $p_{cut}(linker) = 10 \cdot p_{cut}(nuc)$  were deduced from previous MNase footprinting studies (45). Altogether, we modelled 101 cleavage sites, 50 intra-nucleosomal and 51 inter-nucleosomal DNA linker sites. According to the  $p_{cut}(\cdot)$  values, regions were chosen randomly, and if a region was selected by our algorithm, a cut was introduced by labelling the central nucleotide. At the end of the simulation, these labels were used to deduce the number and length of the fragments.

The characteristic difference of our partial (low-MNase concentration) and high (high-MNase concentration) chromatin digestion conditions is reflected by the number of cutting events per template. In accordance with our experimental conditions, we assigned 20 double stranded cutting events for the low and 70 for the high MNase condition in all the computer simulations (Supplementary Fig-

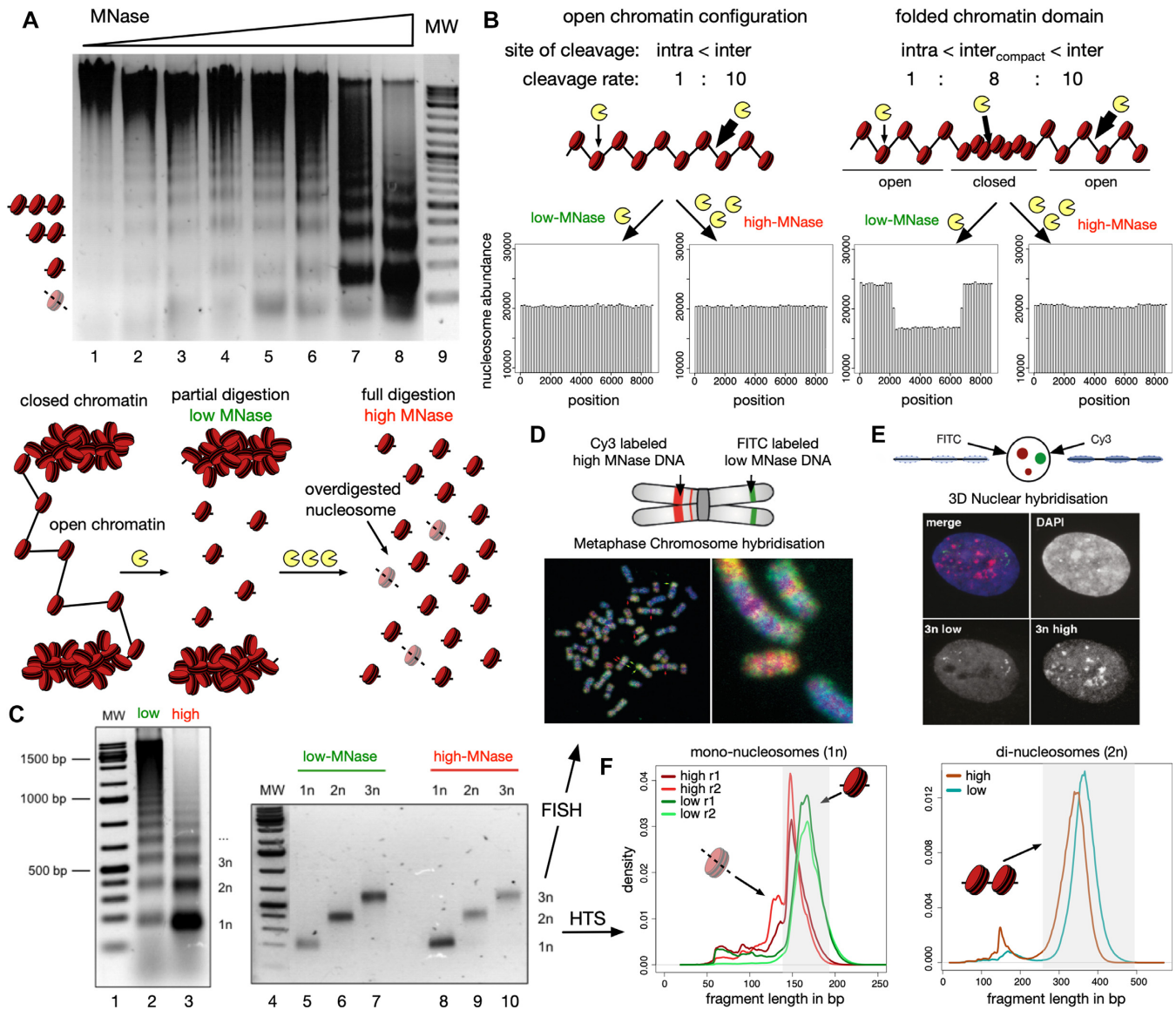


**Figure 1.** Isolation of nucleosomal DNA after differential MNase hydrolysis. (A) Nucleosomal DNA ladder of HeLa cells incubated with increasing concentrations of MNase. The agarose gel is showing the analysis of the purified DNA after MNase hydrolysis. The molecular weight marker is shown in lane 9 and the positions of subnucleosomal, mono-, di- and tri-nucleosomal DNA are indicated. The scheme below illustrates the hypothetical results of a partial and full hydrolysis of differentially accessible chromatin domains. (B) Simulation of low- and high-MNase digestions (see Materials and Methods for details) of an equally accessible linker DNA with  $p_{cut}(linker) = constant$  (left panel) and of a nucleosomal array containing a central compacted chromatin domain with reduced linker accessibility  $p_{cut}(linker, compact) = 0.8 \cdot p_{cut}(linker)$ , (right panel). The relative sensitivity of intra-nucleosomal (intra) and inter-nucleosomal (inter) cleavage is indicated. (C) Large scale low- and high-MNase hydrolysis of chromatin (lanes 2 and 3) and subsequent isolation of nucleosomal DNA corresponding to the mono-, di-, and tri-nucleosomes (lanes 5 to 10). (D, E) 2D and 3D FISH experiments with isolated tri-nucleosomal DNA. Metaphase FISH (D) and 3D FISH (E) were performed with Cy3/FITC labelled tri-nucleosomal DNA derived from high-/low-MNase digestions, as indicated. (F) Low- and high-digested mono- and di-nucleosomal DNA were subjected to library preparation and high throughput sequencing. The fragment size distributions of the mapped paired-end reads for mono- (left panel) and di-nucleosomal DNA (right panel) are shown. The shaded boxes highlight the fraction of isolated mono-nucleosomal (140–200 bp) and di-nucleosomal (250–500 bp) fragments.

ure S1B). The *in silico* MNase digestion of the nucleosomal array was iterated until 1 million mono-nucleosome-sized fragments were collected for each condition. Finally, the location and number of mono-nucleosomal fragments were determined and plotted. As expected, computer simulations modelling at least 20 cutting events resulted in histograms that resembled the nucleosome ladders of our experimental setup (Supplementary Figure S1B and C); these findings confirmed our model and choice of parameters.

We wanted to know how the open and compact chromatin domains would be represented in the high- and low-MNase digestion conditions. Modelling a chromatin domain with identical DNA linker accessibility ( $p_{cut}(linker) = const$ ) throughout the whole nucleosomal array resulted in indistinguishable accessibility patterns at varying MNase digestion conditions (Figure 1B, left panel and Supplementary Figure S2A). However, if we modelled a compacted chromatin domain located at the centre of a chromatin fi-

bre by means of 25 nucleosomes with reduced DNA linker accessibility ( $p_{cut}(linker, compact) = 0.8 \cdot p_{cut}(linker)$ ), we observed striking differences between low and high digestion conditions (Figure 1B, right panel). For high-MNase conditions, which are the standard experimental conditions to study nucleosome occupancy and cellular chromatin structure, modelling resulted in identical patterns. In contrast, strikingly reduced levels of nucleosomal DNA were predicted for the compacted chromatin domains, when we simulated low-MNase conditions (Figure 1B, right panel). Note that this finding does not depend on the chosen parameters: The simulation congruently predicted differences between MNase conditions in the compacted chromatin domain, simulating 10–60% of array cleavage (Supplementary Figure S2B). Furthermore, the low-MNase condition sensitively detected alterations of the linker accessibility, whereas the high-MNase signal was unaffected (Supplementary Figure S2C). Taken together, the outcome of our simulation suggests that low-MNase conditions, in comparison to high-MNase conditions, should reveal differences in hierarchical chromatin organization.

### High- and low-MNase treated chromatin localizes to distinct nuclear compartments

To test our computer modelling experimentally and to annotate chromatin domains, we isolated the mono-, di- and tri-nucleosomal DNA fractions of low- and high-MNase treated cells for FISH (fluorescence *in situ* hybridization) and high-throughput sequencing analysis (Figure 1C–F).

First, we tested whether low- and high-MNase treatment released different fractions of the genome by analysing the tri-nucleosomal DNA in 2D and 3D FISH experiments. FISH is an ideal method to visualize differential genomic locations of DNA in the mega base pair scale by hybridization to metaphase chromosomes (2D FISH), as well as to monitor the compartmentalization of the DNA probes in the nucleus by retaining the 3D structure of the chromosomes in the cell nucleus (3D FISH). The tri-nucleosomal DNA isolated from high- and low-MNase conditions was fluorescently labelled with either Cy3 (high-MNase) or FITC (low-MNase) and subsequently used as probes in 2D and 3D FISH (Figure 1D and E). In 2D, the signals of the high- and low-MNase DNA probes partially overlapped, but large regions with distinct staining patterns could also be detected (Figure 1D). As expected, we observed regions devoid of low-MNase-treated nucleosomal DNA within the centromeric regions of the chromosomes. Additionally, the 3D FISH experiment, maintaining the nuclear architecture in 3D, clearly showed a spatial separation of the chromatin regions extracted with either low- or high-MNase concentrations (Figure 1E). We also performed Southern blot experiments, hybridizing the MNase-treated chromatin with the isolated tri-nucleosomal DNA from high- and low-MNase treatment (Supplementary Figure S3). Hybridizing the high- and low-MNase-treated tri-nucleosomal DNA to nucleosomal ladders showed indistinguishable hybridization patterns. This suggests that differential MNase treatment does not result in a global loss or enrichment of genomic fractions. Therefore, our results indicate that high- and low-MNase extractions do preferen-

tially release different genomic regions, potentially exhibiting distinct DNA packaging properties and localizing to different nuclear compartments in the cell.

### MNase sequence preferences dominate differential chromatin fragmentation

To resolve and map the different chromatin domains at high resolution, we performed high-throughput sequencing with the isolated mono- and di-nucleosomal DNA, extracted with either high- or low-MNase concentrations. Plotting the length distribution of the paired-end sequencing reads showed the expected average DNA fragment length of  $\approx 150$  bp for mono-nucleosomal DNA and  $\approx 340$  bp for di-nucleosomal DNA (Figure 1F). Nucleosomal DNA fragments released by low MNase digestions tend to be slightly larger due to incomplete hydrolysis of the linker DNA. Interestingly, the high-MNase-treated chromatin exhibited an additional fraction of sub-nucleosomal sized fragments, which may represent partially digested nucleosomes (52). For our subsequent analyses, we extracted DNA fragments of 140 to 200 bp for the mono-nucleosomal DNA and 250–500 bp for the di-nucleosomal DNA, yielding in total 393 million annotated mono-nucleosomes and 75 million di-nucleosomes. This read depth allowed us to perform a thorough statistical analysis of genome coverage and subsequent chromatin domain analysis.

Mapping the sequence reads to the human genome (version hg19) was performed and an overview of mono-nucleosomal read distribution is exemplarily given for chromosome 6 (Figure 2A) and the whole genome (Supplementary Figure S4A). The distribution of low- and high-MNase-treated di-nucleosomal DNA reads is shown in Supplementary Figure S4B and C. In both cases, the high- and low-MNase-treated samples revealed a high coverage and a rather similar distribution across the genome. To monitor differential fragment enrichments with respect to low- and high-MNase treatment, the log fold-change in coverage was calculated in 1 Mb non-overlapping windows (Figure 2A, Supplementary Figure S4). Interestingly, as in the FISH experiments, we observed clusters of large, Mb-sized domains, exhibiting either enrichment of high- or low-MNase-treated chromatin fractions. These findings suggest that chromatin fragmentation and the subsequent isolation of mono- and di-nucleosomes gave rise to an enrichment pattern that is specific to the applied MNase concentration.

MNase has a known sequence preference, preferentially hydrolyzing DNA at sites exhibiting A/T nucleotides (52–56). Therefore, we analyzed the GC content of the isolated DNA fragments. Remarkably, genomic regions enriched in the high-MNase digestions showed an increased GC content, whereas the average GC content of the low-MNase-isolated fragments reflected the genome-wide average as indicated by the  $P$ -value = 0.03 of a paired  $t$ -test (Figure 2B). To exclude the possibility that this is a specific characteristic of our experimental approach, we applied the same analysis to previously published data sets obtained from different organisms (31,52). Even though different chromatin extraction protocols have been used, including formaldehyde crosslinking and nuclei isolation steps, the same trend can be observed: The GC content of chromatin released

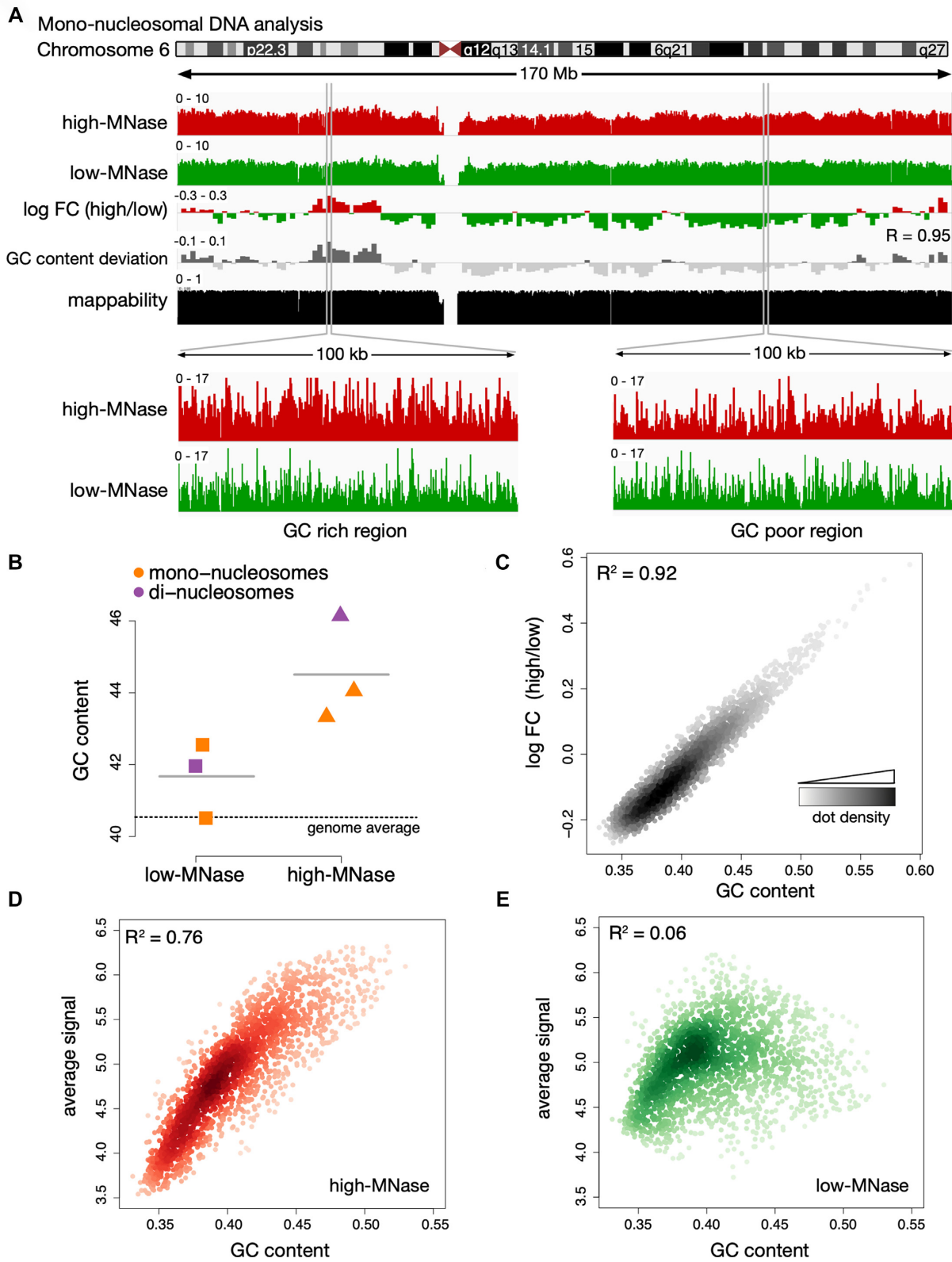


**Figure 2.** MNase sequence preferences dominate differential chromatin fragmentation. (A) Genome browser plot showing the nucleosome occupancy distribution along chromosome 6. Differences of high- and low-MNase digestions were calculated as  $\log_2$  fold changes (log FC) of the average profile intensity in 1 Mb non-overlapping windows. GC content variation is displayed as the deviation from the genome wide average (40.5%). R is the Pearson correlation coefficient determined for the log FC (high/low) and the GC content deviation. The mappability track at the bottom illustrates how uniquely 100mer sequences align to a region of the genome (41). (B) Average GC content of isolated mono- and di-nucleosomal fragments. The genome wide GC average is indicated by the dashed line. (C–E) Genome wide correlation of GC content and nucleosome occupancy profiles. Dots represent 1 Mb non-overlapping windows; the coefficient of determination ( $R^2$ ) refers to the result of a simple linear regression between GC content and the average signal of (C) log FC of high-MNase versus low-MNase, (D) high-MNase, (E) low-MNase.

with high-MNase concentrations is higher, whereas the GC content of low-MNase samples is generally close to the genome-wide GC distribution (Supplementary Figure S5A and B). Furthermore, from those data sets we deduced additional controls following MNase digestion, such as Histone-ChIPs, and confirmed that this effect is not caused by a contamination of non-nucleosomal fragments in the low-MNase condition (Supplementary Figure S5A and B).

To test whether the sequence preference of MNase would mask the identification of chromatin domains, we correlated the log fold-change of high- and low-MNase signals with the underlying GC content. Indeed, we observed a remarkably high correlation between GC content and differences in high- and low-MNase digestion ( $R^2 = 0.92$ , Figure 2C), indicating that the DNA sequence influences the differential chromatin fragmentation (Figure 2A–C, Supplementary Figure S6A and B). The comparison of a GC-poor and a GC-rich genomic region revealed great variations of the high-MNase signals, yielding more reads in high-GC regions and less reads with a more variable read distribution in low-GC regions (Figure 2A, lower panel). The genome-wide correlation analysis indicated a strong correlation between the signal under high-MNase conditions and the GC content ( $R^2 = 0.76$ ) explaining the varying signal intensities (Figure 2D). In contrast, the low-MNase reads did not correlate with GC content ( $R^2 = 0.06$ , Figure 2E). This finding showed that the low-MNase digestion pattern is unaffected by the GC content, giving rise to a homogenous read distribution across the genome. These results were also evident, when we analyzed existing datasets of human cells that were incubated with varying MNase concentrations (5.4–304 units; (33), Supplementary Figure S5C). An additional important observation that can be drawn from the experiments is the absence of GC-bias when low amounts of MNase were used, suggesting that these conditions do represent the overall nucleosome occupancy and positioning the best.

### Nucleosomes of GC-poor genomic regions are under-represented in high-, but not in low-MNase conditions

MNase-dependent sequence bias and the positioning and occupancy of nucleosomes have a strong effect on the dinucleotide frequency repeats of the isolated DNA fragments. Therefore, we wanted to know whether these were equally well represented in our HeLa dataset, assessed at low- and high-MNase conditions. For both low- and high-MNase conditions, we could confirm two typical signatures: First, the overall dinucleotide frequencies within the nucleosomal DNA fragments showed the expected 10 bp phasing of G/C or A/T dinucleotides (57), confirming the proper isolation of nucleosomal DNA (Figure 3A, Supplementary Figure S7). Additionally, we detected the preferential hydrolysis of DNA at A/T sites in isolated DNA fragments (52) (Supplementary Figure S7B).

However, in addition to the local A/T preference of MNase, we observed changes in nucleotide content within the nucleosome core sequence and neighboring regions that differ with the experimental condition. The nucleosomal DNA possessed increased G/C content relative to the genomic G/C content in low-MNase conditions, and this

trend became more prominent in high-MNase conditions (Figure 3A, Supplementary Figure S7A). When using low-MNase conditions, the average G/C content in the linker DNA and surrounding regions matched the genome-wide dinucleotide distribution. In contrast, when using high-MNase conditions we observed an overall increase in the G/C dinucleotide content of the nucleosomal DNA and the surrounding genomic regions. This suggests that high-MNase treatment introduces the preferential selection of GC-rich fragments. This effect can be explained by an increased MNase sensitivity of nucleosomal core DNA reconstituted on AT-rich DNA, being preferentially hydrolyzed and thereby removed from the nucleosomal fraction and analysis (Figure 2A, lower panel).

Next, we addressed whether the observed GC bias in high-MNase digestions would influence the analysis of genome-wide nucleosome positions and occupancy. Therefore, we used the DANPOS package (39) to annotate nucleosome positions from our MNase-seq data. DANPOS identified and annotated fewer nucleosomes in GC-poor regions of high-MNase digestions than with low-MNase treatment (Figure 3B). Among the low-MNase data, the overall number of predicted nucleosomes depended on the underlying GC content and nucleosome prediction was more homogeneous throughout the genome (Figure 3C and D). In line with the observed GC bias in the read distribution of the high-MNase data, we observed that nucleosome annotation is worse in the GC-poor regions.

So far, our computer simulation did not predict a variation in the high-MNase data (Figure 1B), which indicated that a further refinement of our *in silico* approach was required. To model the preferential digestion of nucleosomes occupying AT-rich regions, we introduced an increased nucleosome digestion probability at AT-rich regions  $p_{cut}(nuc, AT^+)$ . The outcome of this refined model resembled our *in vivo* observations at high-MNase-conditions (Figure 3E,  $p_{cut}(nuc, AT^+) = 2 \cdot p_{cut}(nuc)$  used). Now, domains with AT-rich DNA sequences were represented by a loss of extracted nucleosomes at high-MNase conditions. Interestingly, the refinement of the model did not alter nucleosome extractability in the low-MNase conditions. Note that this prediction does not depend on the chosen  $p_{cut}(nuc, AT^+)$  values and is robust even at higher nucleosome cleavage probabilities (Supplementary Figure S8). Our *in silico* results are in agreement with the experimental findings from low-MNase conditions which provide a more regular representation of genome-wide nucleosome positions than the commonly used high-MNase concentrations.

The inherent GC bias, with an increased GC content in the high MNase sample, could interfere with the analysis of domain architecture when compared to the low MNase treated samples. In contrast, the above findings make plausible that low-MNase conditions are sufficient to identify compacted domains of higher-order structures. To confirm this assumption, we compared the low-MNase data with the read distribution of chromatin fragmented by sonication. As shown in Supplementary Figure S9A and B, the datasets are highly correlated ( $R = 0.8$ ); this finding suggests that there are no genomic domains of differential DNA organisation on the mega base pair scale (Mb).



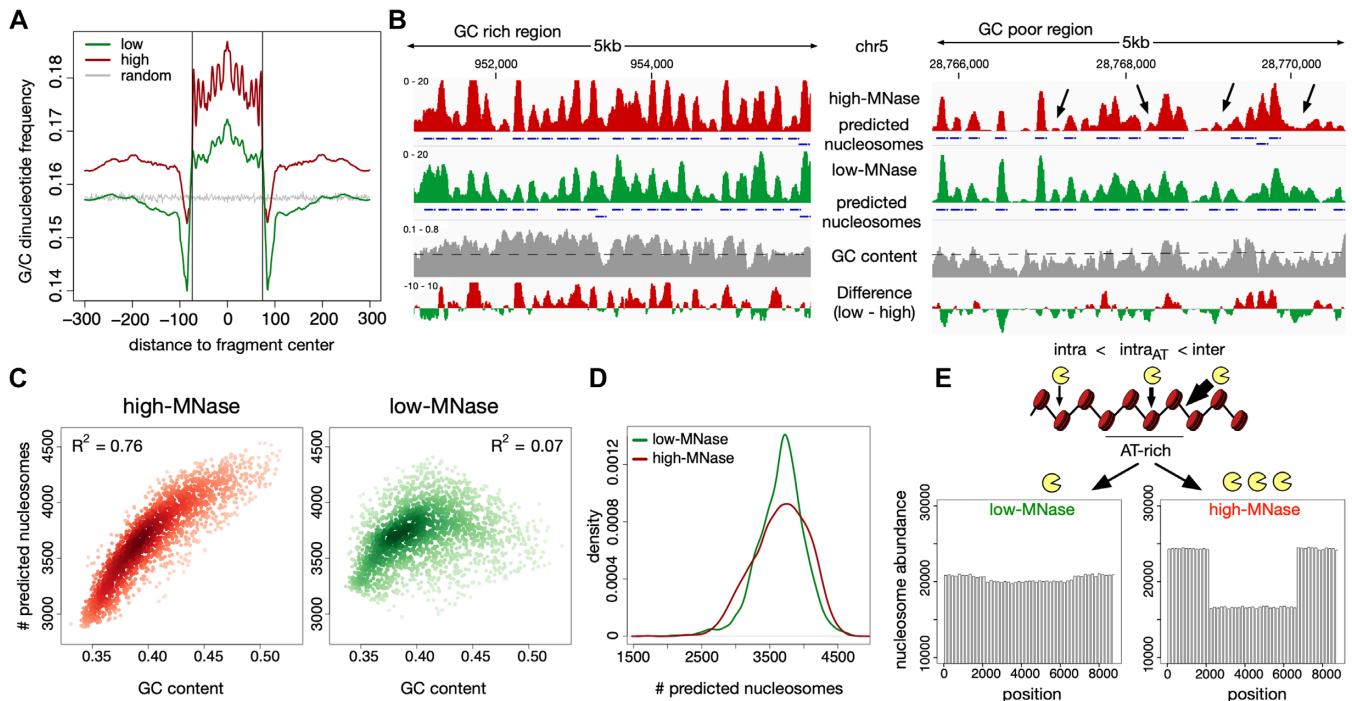


**Figure 3.** Nucleosomes in AT-rich regions are partially depleted in high-, but not in low-MNase conditions. (A) Average G/C-di-nucleotide frequency, deduced from GG, GC, CG, CC occurrences, centred on mapped mono-nucleosomal fragment midpoints. A random distribution (grey) was simulated on 1 million randomly generated fragments of 147 bp lengths. Vertical lines indicate nucleosome boundaries ( $\pm 73$  bp). (B) Genome browser snapshot showing the GC bias of nucleosome annotation after high MNase digestions. Nucleosome positions, which have been called with the DANPOS2 toolkit (80), are represented by blue boxes. Arrows indicate over-digested nucleosomes in high MNase condition. GC content was calculated in 50 bp windows with 10 bp sliding steps. The genome wide GC average is given by the dashed line. (C) Genome wide correlation of GC content and quantity of nucleosome prediction. Dots represent 1 Mb non-overlapping windows; (D) Kernel density plot of the nucleosome count in 1 Mb sized windows. (E) Simulation of low- and high-MNase digestions of a nucleosome strand exhibiting nucleosomes with variable MNase sensitivity. A higher intra-nucleosome cleavage probability  $p_{cut}(nuc, AT^+)$  was assigned to a stretch simulating an AT-rich region in the middle of the chromatin strand. Used cleavage probabilities:  $p_{cut}(nuc, AT^+) = 2 \cdot p_{cut}(nuc)$  and  $p_{cut}(linker) = 10 \cdot p_{cut}(nuc)$ .

### Large domains of differential chromatin organisation are not detectable

Next, we addressed whether differential organisation of chromatin would affect the MNase dependent extraction of DNA in genomic regions that are smaller than the Mb scale. Domains located in open or folded chromatin configurations should modulate DNA accessibility, independent of the underlying GC content. Therefore, we used a sliding window approach and determined the correlation of the low- and high-MNase datasets with the GC content of the corresponding genome sequence. This analysis is based on the assumption that a fraction of the genome should escape the GC content correlation of the low-/high-MNase extraction, if differential chromatin packaging domains exist.

First, correlation was determined for a window size of 1 Mb, which corresponds to a domain of  $\sim 5000$  nucleosomes. The strong conservation ( $R^2 = 0.92$ ) argues against differential chromatin domains of this size (Figure 4A). A pronounced correlation ( $R^2 > 0.44$ ) persisted, even after gradually reducing the scanning window size down to 5 kb, which represents a domain of only 3 solenoidal turns and a total of  $\sim 25$  nucleosomes. Even for a window size of 1 kb which is too small to represent a structural domain, we observed a moderate correlation (Figure 4A, Supplementary Figure S10A).

To directly assess the accessibility of euchromatin and heterochromatin fractions, we then focussed on the annotated regions that can be identified by their post-translational histone modifications. However, due to the dominating GC bias in our analysis, we were not able to correlate differences of low-/high-MNase with histone modifications (Supplementary Figure S10). Therefore, we globally normalized the number of sequencing reads to the GC content of the underlying genomic region. Generally, euchromatin has a higher GC content than heterochromatic regions (58). Thus, we applied a locally weighted scatterplot normalization (LOESS, window size 250 bp) to correct for the genome-wide GC variation (Supplementary Figure S11A). After normalization, the ratio of low- and high-MNase sequencing reads were no longer correlated with GC-content (Supplementary Figure S11B;  $R = 0.02$ ), allowing us to screen for other features that might modulate DNA accessibility.

We first had a closer look at a heterochromatin locus on chromosome 1 that is heavily marked by histone H3K27me3. Visual inspection showed no tendency of particular high-/low-MNase ratio changes within this domain (Figure 4B). This locus was no special case and we observed no correlation of high-/low-MNase ratios with increasing histone H3K27me3 density for a genome-wide screen of this heterochromatin mark (Figure 4C, blue boxplots). In con-

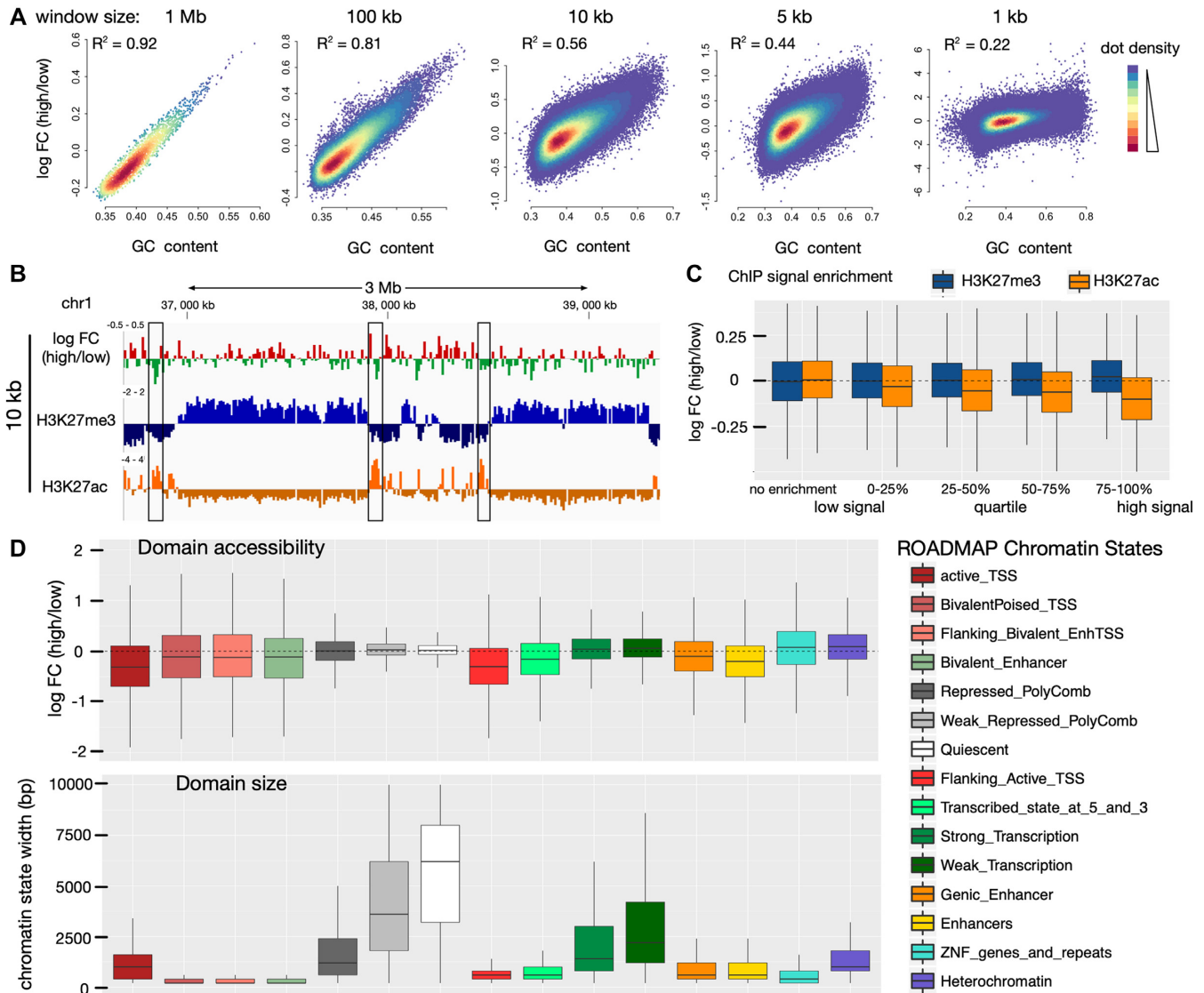


**Figure 4.** Comparison of chromatin accessibility within annotated chromatin regions. (A) Genome wide correlation of GC content and differential MNase signal. Dots represent non-overlapping windows of varying genome sizes (size given at the top). (B) Genome browser snapshot showing H3K27me3 (ENCODE, ENCF958BAN) marked domains and local H3K27ac sites (ENCODE, ENCF311EWS) highlighted by black rectangle compared to differential MNase digestions.  $\log_2$  FC was calculated in 10 kb non-overlapping windows. (C) Correlation of H3K27me3 (blue) / H3K27ac (orange) enrichment over input with differential MNase digestion enrichment. The average signal was calculated in 10 kb non-overlapping windows spanning the whole genome. Windows were grouped on the basis of the ChIP enrichment signal into windows showing no ChIP enrichment (ChIP-signal < input signal) and windows enriched for the histone modification were further subdivided into quartiles of signal enrichment. (D) Differential MNase signal (upper panel) in annotated chromatin states (ROADMAP) compared to the size of the chromatin states (lower panel). (B–D) The MNase signal was normalized for the underlying GC-bias (see Supplementary Figure S11 and Materials and Methods for details).

trast, euchromatic marks such as H3K27ac are not spread over large genomic regions but are locally concentrated (Figure 4B). The selected genomic region was strongly enriched for H3K27ac modifications, overlapping with a domain of increased MNase accessibility (Figure 4B, boxes). This is even true on the genomic scale: With higher densities of the H3K27ac mark, we observed an increased accessibility towards MNase hydrolysis (Figure 4C). This suggests that only highly modified sites like active enhancers show an alteration in the chromatin structure. A recent study by Mieczkowsky *et al.* (33) showed that active and silent chromatin marks can be distinguished by a MNase based acces-

sibility score. The re-analysis of the low and high MNase digestion conditions in human K562 cell line confirm our results (Supplementary Figure S12A). Even the comparison to the fully digested chromatin sample (Supplementary Figure S12A, right panel) showed only a significant increase in MNase accessibility at H3K27ac associated regions, but not for H3K27me3, suggesting that mainly the active mark correlates with differences in chromatin openness.

To elucidate features that might affect the accessibility of chromatin, we statistically analyzed the annotated chromatin states and their genomic regions from the ROADMAP project (48) (Figure 4D). Therefore, the high-

/low-MNase ratio in functionally defined domains of the genome was calculated. Box-plots with negative log FC values are indicative of elements located in more accessible chromatin. These were active Transcription Start Sites (TSS), bivalent poised TSSs, enhancers and regions flanking the active TSSs and transcribed regions. Analysis of domain sizes revealed that these regions ranged from 200 to 1500 bp and showed that chromatin accessibility is regulated at a local scale. In contrast, no compacted genomic regions with decreased MNase sensitivity were detected. The heterochromatic and transcriptionally repressed regions of the genome, encompassing domains of 1000 to 10 000 bp, showed similar MNase accessibility at both low and high enzyme concentrations.

These results were confirmed, when analysing the high and low digestions performed by Mieczkowski and colleagues (33). We showed that it is not required to analyse multiple MNase digestions conditions, as the data do not qualitatively change when comparing different high to low MNase treatment conditions (Supplementary Figure S12B). The analysis is significant by comparing a single high to a single low MNase condition, showing that again the small domains of active TSS, bivalent poised TSSs, enhancers and regions flanking the active TSSs and transcribed regions were MNase hypersensitive. However, the larger regions, irrespective of being euchromatin or heterochromatin domain showed no difference in MNase accessibility (Supplementary Figure S12B).

Taken together, these analyses, which were deduced from large (>1.5 kb) genomic regions, suggest a homogeneous accessibility of chromatin that does not depend on histone modification patterns or functional domains of the genome. As a consequence, we postulate that independent of the marking or activity of the genomic regions the degree of DNA packaging is the same.

### Chromatin accessibility is modulated on local scale

As we observed differential chromatin packaging at the local scale, we performed a detailed analysis of the low-/high-MNase data sets at the nucleosomal level. Sliding windows as small as 1 kb exhibited a decreased GC correlation (Figure 4A, Supplementary Figure S10B and C). Remarkably, sites showing an enrichment in the low-MNase fraction coincided with DNase I HS sites and/or active histone marks as H3K27ac near actively transcribed genes. Visual inspection revealed an enrichment of nucleosomes released under low-MNase conditions at those sites (Figure 5A, Supplementary Figure S10B and C), suggesting the existence of local hyper-accessible sites.

Next, we correlated the nucleosome profile of either high- or low-MNase digestions with annotated DNase I HS in HeLa cells from the ENCODE project (48). Though the GC content at DNase I HS is higher than the genome-wide average, our analysis showed an enrichment of the low-MNase fractions, indicating that nucleosomes at these sites adopt an open chromatin configuration (Figure 5A and B). Interestingly, only nucleosomes coinciding with or adjacent to the DNase I HS showed a significant enrichment, suggesting local modulation of chromatin accessibility. In addition, the MNase sequence bias within the high-MNase dataset

would result in an underestimation of accessible nucleosome enrichment. Therefore, we corrected GC enrichment by using a LOESS normalization as described above (see above and Methods for details, Supplementary Figure S11). We applied the *Dpeak* script from the *DANPOS2* toolkit to the normalized data in order to identify differentially enriched sites in the low- and high-MNase fractions. In the genome wide analysis, 36433 sites revealed a significant enrichment in low-MNase nucleosomes and were termed as MNase hyper-accessible sites. In addition, we identified 35454 sites with significant enrichment in high-MNase nucleosomes, termed MNase inaccessible sites (Supplementary Figure S13A and B). In contrast to MNase inaccessible sites, MNase hyper-accessible sites coincide with the annotated DNase I HS ( $P$ -value  $< 2.2 \cdot 10^{16}$  Fisher's exact test, Supplementary Figure S13B). Although we observed only a partial overlap, DNase I HS coinciding with MNase hyper-accessible sites exhibited a high signal intensity in DNase I HS assays (Supplementary Figure S13C). Furthermore, MNase hyper-accessible sites were enriched at gene regulatory elements, such as active TSS and predominantly enhancers, indicating a link between local chromatin accessibility and gene regulation (Supplementary Figure S13D). In summary, our data suggests that the nucleosomal array structure is exposed only locally, potentially allowing for the binding of regulatory factors.

### MNase-sensitive nucleosomes occupy hyper-accessible sites

A recent study using a chemical approach to map nucleosomes in mouse embryonic stem cells identified histone binding at regulatory sites, that have previously been suggested to be nucleosome-free in genome-wide MNase-seq studies (59). However, the functional implication of these sites is still unclear, as highly MNase sensitive nucleosomes were found at repressed promoters of stress response genes and at the promoters of highly active genes (60,61). Here we show that our low MNase treatment condition is well suited to identify the fragile nucleosomes, that are well-positioned upstream of active TSSs (Figure 5C). Presumably, these nucleosomes have escaped previous MNase-seq studies which used MNase conditions that we describe as high-MNase.

Accordingly, the centres of active enhancers in HeLa cells were depleted of nucleosomes in the high-MNase fraction, whereas in low-MNase fractions these nucleosomes were markedly enriched (Figure 5D). Even directly at CTCF-bound sites we detected MNase-sensitive nucleosomes, which were preferentially degraded in high-MNase conditions (Figure 5E). In contrast to a model, where CTCF and nucleosomes compete for DNA binding, we observed the highest nucleosome enrichment in low-MNase at sites exhibiting strong CTCF-ChIP signals (Figure 5F). Together, these results indicate that it may not be required to reposition or deplete nucleosomes for factor binding.

Additional computer simulations confirmed our *in vivo* observations (Figure 5G). We introduced a nucleosome with an enhanced probability of an intra-nucleosome cleavage ( $p_{cut}(nuc, fragile) = 4 \cdot p_{cut}(nuc)$ ), surrounded by two hyper-accessible inter-nucleosome cleavage sites ( $p_{cut}(linker, hyper-accessible) = 1.2 \cdot p_{cut}(linker)$ ) to our *in silico* model. This small adaptation was sufficient to

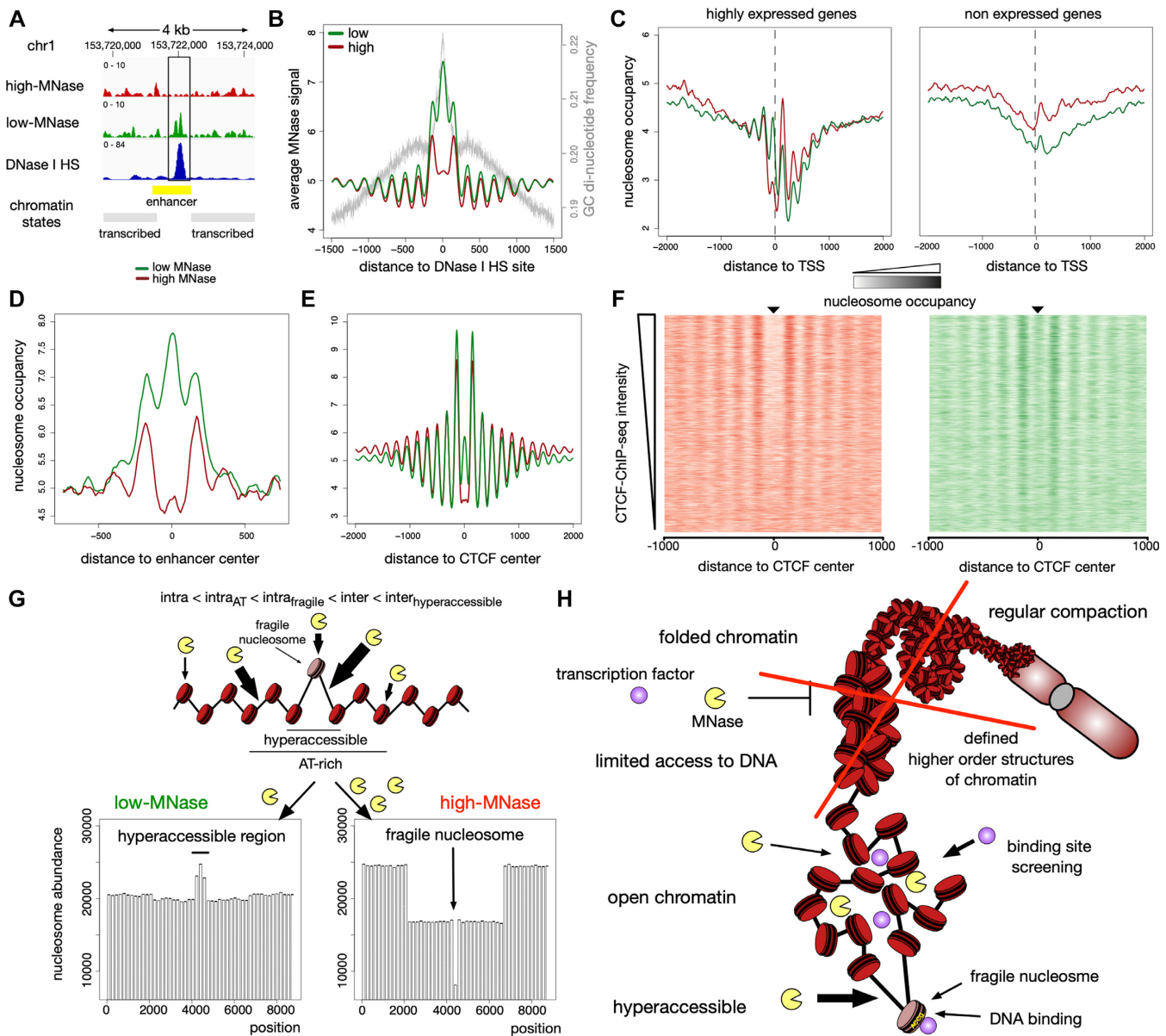


**Figure 5.** Differences of low- and high-MNase analysis at local sites. (A) Genome browser snapshot around an accessible enhancer marked by DNase I HS peak (ENCODE, ENCF567PRQ). (B–E) Averaged MNase-seq profiles around: (B) DNase I HS sites (ENCODE, ENCF692NCU); average G/C—di-nucleotide content is indicated by the grey line. (C) TSS of highly expressed genes (left panel) and not expressed genes (right panel). FPKM values determined by RNA-Seq analysis (ENCODE, ENCF000DNW) were used to estimate the level of gene expression. Genes not detected in RNA-Seq analysis (FPKM = 0) were considered as not expressed and those genes showing the 25% highest FPKM values were considered as highly expressed. (D) Active enhancer sites in HeLa cells as defined in (49). (E) CTCF sites (ENCODE, ENCF002DCW). (F) Heatmaps of high-MNase (left panel) and low-MNase (right panel) are centred on CTCF binding sites and sorted in descending order of ChIP-Seq density at detected CTCF sites. (G) Simulation of low- and high-MNase digestions of a nucleosome array exhibiting nucleosomes with variable MNase sensitivity and hyper-accessible DNA sites. A higher intra-nucleosome cleavage probability  $p_{cut}(nuc, AT^+)$  was assigned to a domain, simulating an AT-rich region in the middle of the chromatin strand. In the centre of the nucleosomal array an hyper-accessible site was introduced, representing a fragile nucleosome with markedly increased intra-nucleosome cleavage probability  $p_{cut}(nuc, fragile)$ , and the two adjacent DNA linker sites were assigned with enhanced inter-nucleosomal cleavage probability  $p_{cut}(linker, hyperaccessible)$ . Chosen cleavage probabilities:  $p_{cut}(nuc, AT^+) = 2 \cdot p_{cut}(nuc)$ ,  $p_{cut}(nuc, fragile) = 4 \cdot p_{cut}(nuc)$ ,  $p_{cut}(linker) = 10 \cdot p_{cut}(nuc)$ ,  $p_{cut}(linker, hyperaccessible) = 12 \cdot p_{cut}(nuc)$ . (H) Schematic model summarising the results of this study.

reproduce MNase-sensitive nucleosomes and local hyper-accessible sites observed *in vivo*.

## DISCUSSION

In the present study, we used differential MNase treatment of cellular chromatin and sequencing of the released mono- and di-nucleosomal DNA to study the overall architecture of the packaged genome. Our results reveal that after normalizing for the genomic GC content, no domains with increased or decreased DNA accessibility can be detected, except for the known local distortions at regulatory regions. In the size range of a few kilo base pairs to mega base pairs the DNA is similarly accessible to MNase hydrolysis throughout the genome. This suggests no differences chromatin packaging, arguing against the proposed hierarchical organisation of chromatin structure. Characterizing and correlating different epigenomic features such as histone marks and functional DNA elements with their respective MNase accessibility, also did not uncover significant differences in DNA accessibility. The only exceptions are local MNase hypersensitive sites at active regulatory regions, but already the nucleosome adjacent to the hypersensitive site revealed the global MNase sensitivity. Taken together, our data suggests that chromatin domains in between the regulatory regions are not organized into distinct hierarchical layers of DNA packaging that would progressively decrease the accessibility of DNA. Meaning also that DNA accessibility in heterochromatin fully resembles the accessibility in euchromatin domains or transcribed regions.

Our results confirm microscopy studies, revealing the absence of regular nuclear patterns that could be interpreted as higher-order structures of chromatin. McDowell and colleagues visualized a homogenous grainy texture of chromosomes, interpreted as 11 nm fibres, lacking areas of hierarchical folding of the nucleosomal chain (62). Additionally, a recent study showed evidence for the lack of domains with distinct higher-order structures of chromatin (17). This ChromEMT method beautifully showed that irregular chromatin polymers, with a diameter of 5–24 nm, exist throughout the cell cycle. The irregular polymers are present at higher or lower concentrations within different nuclear areas and are highly concentrated within the mitotic chromosomes. In addition to changes in polymer concentration, chromatin did not form specific domains with regular folding in the nucleus (17), suggesting the absence of defined higher structures of chromatin. Our study further shows that also within domains of specific epigenetic modifications or genomic functions, no relative difference in DNA accessibility was detected. This gives support for a model in which, for example euchromatin and heterochromatin domains, with distinct transcriptional activity, do not differ in DNA accessibility. Given the study by Ou and colleagues, which suggests that chromatin domains differ in their local concentration of chromatin (17), and the fact that MNase is a small endonuclease, we assume that the enzyme diffuses equally well into all domains of high and low chromatin concentration within the cell. A lack of qualitative differences in MNase dependent cleavage differences implies that there is no distinct structural organization correlating with chromatin density. In

line with these results, super-resolution microscopy showed that chromatin exhibits differences in compaction, with less compact chromatin coinciding with active histone marks and more compact chromatin areas correlating with inactive histone marks (63). These findings indicate that the accessibility of DNA to small sequence specific DNA binding factors is similar throughout the genome, arguing against chromatin folding as a mechanism to regulate DNA accessibility and gene activity (Figure 5H).

Our study supports the absence of regularly folded chromatin in large domains but lacks resolution in the size range of one to six nucleosomes, representing one solenoidal turn. Other studies bridged this gap, like the RICC-Seq assay of the Greenleaf lab (64). They were using radiation damage of DNA and correlated the damage sites with respect to nucleosome array folding, revealing that in heterochromatin damage patterns correlated with a compact two start helical fibre (64). Still, cryo-electron tomography (Cryo-ET), a method that is powerful in revealing repeating structures, failed to detect regular structures in the size range of a few nucleosomes in the nucleus (65), leaving the question open of whether any regular chromatin structure exists. A lack of defined chromatin structure raises the question of how chromatin can fulfill its regulatory function and establish defined compartments within the cell. Our data is in good agreement with the polymer melt model presented by Maeshima *et al.* using fluorescently tagged histones and cryo-electron microscopy to study the chromatin architecture (13,66). The concept of a polymer melt-like structure suggests that the nucleosome fibres are constantly moving and rearranging. High local nucleosome concentrations and interdigitating protein complexes would compete with the formation of regular higher-order structures (67). Our MNase approach ruled out the possibility that the large tag of the fluorescently tagged histone would interfere with the regular folding of chromatin. Taken together, these studies suggest the absence of regular 30 nm fibres and additional higher order structures. However, the ChromEMT study showed, by maintaining the 3D structure of the nucleus, that different parts of the nucleosomal arrays do not directly interact or interdigitate, thereby disturbing the regular path of the fibres (17). The fibres are clearly separated in space and theoretically, the isolated fibres should be able to form intra-nucleosomal interactions and regular higher order structures. The absence of fibre contacts suggests that other mechanisms hinder the proper folding of chromatin, which is observed in *in vitro* experiments (4,5,68,69). We recently showed that chromatin-associated RNA plays an important role in maintaining chromatin accessible. RNase treatment of intact nuclei resulted in the compaction of chromatin and a dramatic reduction in MNase accessibility (70). We concluded that chromatin bound RNA would inhibit the folding of chromatin into defined higher-order structures. With our new study, we would extend this interpretation: We suggest that chromatin-associated RNAs may also regulate the local chromatin density in the cell and more generally interfere with the regular folding of the chromatin fibre. Negatively charged RNA molecules could regulate local chromatin density by a simple charge repulsion mechanism and maintain the nucleosomal arrays at distance and dynamic. Regions of distinct chromatin density,

as revealed by ChromEMT, may represent different RNA pools or RNA concentrations associated with chromatin.

Bringing together the irregular, non-structured nature of cellular chromatin, the binding of RNA, the local differences of chromatin density and the characterized epigenomic domains (48), a previously described buoy model offers an attractive explanation for the regulation of DNA-dependent processes in the cell (71). It proposes that the regulation of chromatin domains does not occur at the level of regular structure, but on the level of chromatin density. Small regulatory DNA binding factors, in the size range of the enzyme MNase, would be capable to access dense chromatin domains without hindrance. However, large multi-protein complexes such as the replication and transcription machinery would be expelled from these domains. For example, pioneering transcription factors could migrate into chromatin domains, identify regulatory regions and bind to them. These sites would now, due to transcription factor recruitment and the associated changes in the physicochemical properties of this region, similar to a buoy show up on the surface of the chromatin domain. At the surface of the dense chromatin domain, this genomic region could now be integrated into the large replication or transcription factories. Molecular sieves could have regulatory potential in combination with local, accessible regions, however, further studies are needed to test these models.

Nucleosome free regions (NFR) at active promoters were defined by their accessibility to MNase and suggested to have nucleosomes replaced by DNA binding factors (72,73). Alternatively it is possible that these sites are covered by a species of fragile nucleosomes that were suggested by the He, Shore and Henikoff labs (32,60,61). Indicative of histone binding at these MNase sensitive regions was a crosslinking study, showing H4 binding at these sites cells (74) and MNase sensitive nucleosomes were also detected at termination sites (73). This opens the possibility that the accessible sites we detected, either harbour MNase-sensitive nucleosomes, or complexes of DNA binding factors that give rise to sensitive nucleosome sized DNA fragments upon MNase hydrolysis. Even though we cannot discriminate between these two options, we show that using low MNase concentrations is the ideal method to circumvent the GC-bias of the common chromatin digestion to mononucleosomes, clearly improving genome wide nucleosome coverage and revealing nucleosome-sized DNA fragments at the previously denominated NFRs. Taken together, we suggest that MNase sensitive nucleosomes locally occupy these active genomic regions and probably co-occupy these sites with DNA binding factors such as CTCF. Nucleosomal MNase sensitivity could be a result of (a) active nucleosome remodelling and high turn-over, as catalyzed by the remodelling enzyme RSC (61); (b) the active incorporation of histone variants such as H3.3 and H2A.Z that could destabilize promoter nucleosomes (75,76); (c) histone modifications that increase DNA breathing and octamer stability (77,78); or (d) being an effect of an altered nucleosome structure, as described by Allfrey and colleagues (79). The nature of these unstable nucleosomes still must be determined biochemically, but intriguingly they appear as individual particles localized in between non-sensitive histone octamers.

## DATA AVAILABILITY

MNase-seq data has been submitted to NCBI Gene Expression Omnibus (GEO; <http://www.ncbi.nlm.nih.gov/geo/>) under accession number GSE100401.

## SUPPLEMENTARY DATA

Supplementary Data are available at NAR Online.

## ACKNOWLEDGEMENTS

We thank Thomas Cremer and Irina Solovei for their help in imaging.

## FUNDING

This study was funded by the DFG (SFB960) and the BMBF (01DN17003). Funding for open access charge: University Funding.

*Conflict of interest statement.* None declared.

## REFERENCES

- Prunell, A. and Kornberg, R.D. (1982) Variable center to center distance of nucleosomes in chromatin. *J. Mol. Biol.*, **154**, 515–523.
- Compton, J.L., Bellard, M. and Chambon, P. (1976) Biochemical evidence of variability in the DNA repeat length in the chromatin of higher eukaryotes. *Proc. Natl. Acad. Sci. U.S.A.*, **73**, 4382–4386.
- Woodcock, C.L. and Ghosh, R.P. (2010) Chromatin higher-order structure and dynamics. *Cold Spring Harb. Perspect. Biol.*, **2**, a000596.
- Robinson, P.J.J., Fairall, L., Huynh, V.A.T. and Rhodes, D. (2006) EM measurements define the dimensions of the ‘30-nm’ chromatin fiber: evidence for a compact, interdigitated structure. *Proc. Natl. Acad. Sci. U.S.A.*, **103**, 6506–6511.
- Schalch, T., Duda, S., Sargent, D.F. and Richmond, T.J. (2005) X-ray structure of a tetranucleosome and its implications for the chromatin fibre. *Nature*, **436**, 138–141.
- Song, F., Chen, P., Sun, D., Wang, M., Dong, L., Liang, D., Xu, R.-M., Zhu, P. and Li, G. (2014) Cryo-EM study of the chromatin fiber reveals a double helix twisted by tetranucleosomal units. *Science*, **344**, 376–380.
- Horowitz, R.A., Agard, D.A., Sedat, J.W. and Woodcock, C.L. (1994) The three-dimensional architecture of chromatin in situ: electron tomography reveals fibers composed of a continuously variable zig-zag nucleosomal ribbon. *J. Cell Biol.*, **125**, 1–10.
- Scheffer, M.P., Eltsov, M. and Frangakis, A.S. (2011) Evidence for short-range helical order in the 30-nm chromatin fibers of erythrocyte nuclei. *Proc. Natl. Acad. Sci. U.S.A.*, **108**, 16992–16997.
- Fussner, E., Djuric, U., Strauss, M., Hotta, A., Perez-Iratxeta, C., Lanner, F., Dilworth, F.J., Ellis, J. and Bazett-Jones, D.P. (2011) Constitutive heterochromatin reorganization during somatic cell reprogramming. *EMBO J.*, **30**, 1778–1789.
- Ricci, M.A., Manzo, C., Garcia-Parajo, M.F., Lakadamyali, M. and Cosma, M.P. (2015) Chromatin fibers are formed by heterogeneous groups of nucleosomes in vivo. *Cell*, **160**, 1145–1158.
- Joti, Y., Hikima, T., Nishino, Y., Kamada, F., Hihara, S., Takata, H., Ishikawa, T. and Maeshima, K. (2012) Chromosomes without a 30-nm chromatin fiber. *Nucleus*, **3**, 404–410.
- Chen, C., Lim, H.H., Shi, J., Tamura, S., Maeshima, K., Surana, U. and Gan, L. (2016) Budding yeast chromatin is dispersed in a crowded nucleoplasm in vivo. *Mol. Biol. Cell*, **27**, 3357–3368.
- Eltsov, M., MacLellan, K.M., Maeshima, K., Frangakis, A.S. and Dubochet, J. (2008) Analysis of cryo-electron microscopy images does not support the existence of 30-nm chromatin fibers in mitotic chromosomes in situ. *Proc. Natl. Acad. Sci. U.S.A.*, **105**, 19732–19737.
- Fussner, E., Strauss, M., Djuric, U., Li, R., Ahmed, K., Hart, M., Ellis, J. and Bazett-Jones, D.P. (2012) Open and closed domains in the mouse genome are configured as 10-nm chromatin fibres. *EMBO Rep.*, **13**, 992–996.

15. Hsieh, T.-H.S., Weiner, A., Lajoie, B., Dekker, J., Friedman, N. and Rando, O.J. (2015) Mapping nucleosome resolution chromosome folding in Yeast by Micro-C. *Cell*, **162**, 108–119.
16. Nozaki, T., Imai, R., Tanbo, M., Nagashima, R., Tamura, S., Tani, T., Joti, Y., Tomita, M., Hibino, K., Kanemaki, M.T. *et al.* (2017) Dynamic organization of chromatin domains revealed by super-resolution live-cell imaging. *Mol. Cell*, **67**, 282–293.
17. Ou, H.D., Phan, S., Deerinck, T.J., Thor, A., Ellisman, M.H. and O’Shea, C.C. (2017) ChromEMT: Visualizing 3D chromatin structure and compaction in interphase and mitotic cells. *Science*, **357**, eaag0025.
18. Grigoryev, S.A., Bascom, G., Buckwalter, J.M., Schubert, M.B., Woodcock, C.L. and Schlick, T. (2016) Hierarchical looping of zigzag nucleosome chains in metaphase chromosomes. *Proc. Natl. Acad. Sci. U.S.A.*, **113**, 1238–1243.
19. Marsden, M.P. and Laemmli, U.K. (1979) Metaphase chromosome structure: evidence for a radial loop model. *Cell*, **17**, 849–858.
20. Fisher, E.A. and Felsenfeld, G. (1986) Comparison of the folding of beta-globin and ovalbumin gene containing chromatin isolated from chicken oviduct and erythrocytes. *Biochemistry*, **25**, 8010–8016.
21. Caplan, A., Kimura, T., Gould, H. and Allan, J. (1987) Perturbation of chromatin structure in the region of the adult beta-globin gene in chicken erythrocyte chromatin. *J. Mol. Biol.*, **193**, 57–70.
22. Gilbert, N., Boyle, S., Fiegler, H., Woodfine, K., Carter, N.P. and Bickmore, W.A. (2004) Chromatin architecture of the human genome: gene-rich domains are enriched in open chromatin fibers. *Cell*, **118**, 555–566.
23. Naughton, C., Avlonitis, N., Corless, S., Prendergast, J.G., Mati, I.K., Eijk, P.P., Cockroft, S.L., Bradley, M., Ylstra, B. and Gilbert, N. (2013) Transcription forms and remodels supercoiling domains unfolding large-scale chromatin structures. *Nat. Struct. Mol. Biol.*, **20**, 387–395.
24. Hu, Y., Kireev, I., Plutz, M., Ashourian, N. and Belmont, A.S. (2009) Large-scale chromatin structure of inducible genes: transcription on a condensed, linear template. *J. Cell Biol.*, **185**, 87–100.
25. Schones, D.E., Cui, K., Cuddapah, S., Roh, T.-Y., Barski, A., Wang, Z., Wei, G. and Zhao, K. (2008) Dynamic regulation of nucleosome positioning in the human genome. *Cell*, **132**, 887–898.
26. Schones, D.E. (2011) Regulation of nucleosome landscape and transcription factor targeting at tissue-specific enhancers by BRG1. *Genome Res.*, **21**, 1650.
27. Teif, V.B., Vainshtein, Y., Caudron-Herger, M., Mallm, J.-P., Marth, C., Höfer, T. and Rippe, K. (2012) Genome-wide nucleosome positioning during embryonic stem cell development. *Nat. Struct. Mol. Biol.*, **19**, 1185–1192.
28. Moshkin, Y.M., Chalkley, G.E., Kan, T.W., Reddy, B.A., Ozgur, Z., van Ijcken, W.F.J., Dekkers, D.H.W., Demmers, J.A., Travers, A.A. and Verrijzer, C.P. (2012) Remodelers organize cellular chromatin by counteracting intrinsic histone-DNA sequence preferences in a Class-Specific manner. *Mol. Cell Biol.*, **32**, 675–688.
29. Diermeier, S., Kolovos, P., Heizinger, L., Schwartz, U., Georgomanolis, T., Zirkel, A., Wedemann, G., Grosveld, F., Knoch, T.A., Merkl, R. *et al.* (2014) TNF $\alpha$  signalling primes chromatin for NF- $\kappa$ B binding and induces rapid and widespread nucleosome repositioning. *Genome Biol.*, **15**, 536.
30. Valouev, A., Johnson, S.M., Boyd, S.D., Smith, C.L., Fire, A.Z. and Sidow, A. (2011) Determinants of nucleosome organization in primary human cells. *Nature*, **474**, 516–520.
31. Chereji, R.V., Kan, T.-W., Grudniewska, M.K., Romashchenko, A.V., Berezikov, E., Zhimulev, I.F., Guryev, V., Morozov, A.V. and Moshkin, Y.M. (2015) Genome-wide profiling of nucleosome sensitivity and chromatin accessibility in *Drosophila melanogaster*. *Nucleic Acids Res.*, **44**, 1036–1051.
32. Henikoff, J.G., Belsky, J.A., Krassovsky, K., MacAlpine, D.M. and Henikoff, S. (2011) Epigenome characterization at single base-pair resolution. *Proc. Natl. Acad. Sci. U.S.A.*, **108**, 18318–18323.
33. Mieczkowski, J., Cook, A., Bowman, S.K., Mueller, B., Alver, B.H., Kundu, S., Deaton, A.M., Urban, J.A., Larschan, E., Park, P.J. *et al.* (2016) MNase titration reveals differences between nucleosome occupancy and chromatin accessibility. *Nat. Commun.*, **7**, 11485.
34. Stewart, A.F., Reik, A. and Schütz, G. (1991) A simpler and better method to cleave chromatin with DNase I for hypersensitive site analyses. *Nucleic Acids Res.*, **19**, 3157.
35. Cremer, M., Grasser, F., Lanctôt, C., Müller, S., Neusser, M., Zinner, R., Solovei, I. and Cremer, T. (2008) Multicolor 3D fluorescence in situ hybridization for imaging interphase chromosomes. *Methods Mol. Biol.*, **463**, 205–239.
36. Langmead, B. and Salzberg, S.L. (2012) Fast gapped-read alignment with Bowtie 2. *Nat. Methods*, **9**, 357–359.
37. Li, H., Handsaker, B., Wysoker, A., Fennell, T., Ruan, J., Homer, N., Marth, G., Abecasis, G., Durbin, R. and 1000 Genome Project Data Processing Subgroup (2009) The sequence Alignment/Map format and SAMtools. *Bioinformatics*, **25**, 2078–2079.
38. Quinlan, A.R. and Hall, I.M. (2010) BEDTools: a flexible suite of utilities for comparing genomic features. *Bioinformatics*, **26**, 841–842.
39. Chen, K., Xi, Y., Pan, X., Li, Z., Kaestner, K., Tyler, J., Dent, S., He, X. and Li, W. (2013) DANPOS: dynamic analysis of nucleosome position and occupancy by sequencing. *Genome Res.*, **23**, 341–351.
40. Boeva, V., Popova, T., Bleakley, K., Chiche, P., Cappo, J., Schleiermacher, G., Janoueix-Lerosey, I., Delattre, O. and Barillot, E. (2012) Control-FREEC: a tool for assessing copy number and allelic content using next-generation sequencing data. *Bioinformatics*, **28**, 423–425.
41. Derrien, T., Estellé, J., Marco Sola, S., Knowles, D.G., Raineri, E., Guigó, R. and Ribeca, P. (2012) Fast computation and applications of genome mappability. *PLoS One*, **7**, e30377.
42. R Core Team (2014) R: A language and environment for statistical computing. *R Foundation for Statistical Computing*. Vienna, <http://www.R-project.org/>.
43. Schwalb, B., Torkler, P., Duemcke, S., Demel, C., Ripley, B. and Venables, B. (2018) LSD: lots of superior depictions. R package version 3.0. <https://cran.r-project.org/web/packages/LSD/>.
44. Heinz, S., Benner, C., Spann, N., Bertolino, E., Lin, Y.C., Laslo, P., Cheng, J.X., Murre, C., Singh, H. and Glass, C.K. (2010) Simple combinations of lineage-determining transcription factors prime cis-regulatory elements required for macrophage and B cell identities. *Mol. Cell*, **38**, 576–589.
45. Cockell, M., Rhodes, D. and Klug, A. (1983) Location of the primary sites of micrococcal nuclease cleavage on the nucleosome core. *J. Mol. Biol.*, **170**, 423–446.
46. ENCODE Project Consortium, Bernstein, B., Birney, E., Dunham, I., Green, E.D., Gunter, C. and Snyder, M. (2012) An integrated encyclopedia of DNA elements in the human genome. *Nat. Cell Biol.*, **489**, 57–74.
47. Sloan, C.A., Chan, E.T., Davidson, J.M., Malladi, V.S., Strattan, J.S., Hitz, B.C., Gabdank, I., Narayanan, A.K., Ho, M., Lee, B.T. *et al.* (2016) ENCODE data at the ENCODE portal. *Nucleic Acids Res.*, **44**, D726–D732.
48. Roadmap Epigenomics Consortium, Meuleman, W., Bilenky, M., Yen, A., Heravi-Moussavi, A., Kheradpour, P., Zhang, Z., Wang, J., Amin, V., Whitaker, J.W. *et al.* (2015) Integrative analysis of 111 reference human epigenomes. *Nature*, **518**, 317–330.
49. Chen, Y., Pai, A.A., Herudek, J., Lubas, M., Meola, N., Järvelin, A.I., Andersson, R., Pelechano, V., Steinmetz, L.M., Jensen, T.H. *et al.* (2016) Principles for RNA metabolism and alternative transcription initiation within closely spaced promoters. *Nat. Genet.*, **48**, 984–994.
50. Noll, M., Noll, M., Thomas, J., Thomas, J.O. and Kornberg, R.D. (1975) Preparation of native chromatin and damage caused by shearing. *Science*, **187**, 1203–1206.
51. Muyldermans, S., Lasters, I., Hamers, R. and Wyns, L. (1985) Assembly of oligonucleosomes into a limit series of multimeric higher-order chromatin structures. *Eur. J. Biochem.*, **150**, 441–446.
52. Ishii, H., Kadonaga, J.T. and Ren, B. (2015) MPE-seq, a new method for the genome-wide analysis of chromatin structure. *Proc. Natl. Acad. Sci. U.S.A.*, **112**, 3457–3465.
53. Hörz, W. and Altenburger, W. (1981) Sequence specific cleavage of DNA by micrococcal nuclease. *Nucleic Acids Res.*, **9**, 2643–2658.
54. Dingwall, C., Lomonosoff, G.P. and Laskey, R.A. (1981) High sequence specificity of micrococcal nuclease. *Nucleic Acids Res.*, **9**, 2659–2673.
55. Flick, J.T., Eissenberg, J.C. and Elgin, S.C.R. (1986) Micrococcal nuclease as a DNA structural probe: its recognition sequences, their genomic distribution and correlation with DNA structure determinants. *J. Mol. Biol.*, **190**, 619–633.
56. McGhee, J.D. and Felsenfeld, G. (1983) Another potential artifact in the study of nucleosome phasing by chromatin digestion with micrococcal nuclease. *Cell*, **32**, 1205–1215.
57. Kaplan, N., Moore, I.K., Moore, I.K., Fondufe-Mittendorf, Y., Fondufe-Mittendorf, Y., Gossett, A.J., Gossett, A.J., Tillo, D., Field, Y.,

- Field, Y. *et al.* (2009) The DNA-encoded nucleosome organization of a eukaryotic genome. *Nature*, **458**, 362–366.
58. Comings, O.E., Kovacs, B.W., Avelino, E. and Harris, D.C. (1975) Mechanisms of chromosome banding. V. Quinacrine banding. *Chromosoma*, **50**, 111–114.
59. Voong, L.N., Xi, L., Sebeson, A.C., Xiong, B., Wang, J.-P. and Wang, X. (2016) Insights into nucleosome organization in mouse embryonic stem cells through chemical mapping. *Cell*, **167**, 1555–1570.
60. Xi, Y., Yao, J., Chen, R., Li, W. and He, X. (2011) Nucleosome fragility reveals novel functional states of chromatin and poises genes for activation. *Genome Res.*, **21**, 718–724.
61. Kubik, S., Bruzzone, M.J., Jacquet, P., Falcone, J.-L., Rougemont, J. and Shore, D. (2015) Nucleosome stability distinguishes two different promoter types at all Protein-Coding genes in Yeast. *Mol. Cell*, **60**, 422–434.
62. McDowall, A.W., Smith, J.M. and Dubochet, J. (1986) Cryo-electron microscopy of vitrified chromosomes in situ. *EMBO J.*, **5**, 1395–1402.
63. Xu, J., Ma, H., Jin, J., Uttam, S., Fu, R., Huang, Y. and Liu, Y. (2018) Super-Resolution imaging of Higher-Order chromatin structures at different epigenomic states in single mammalian cells. *Cell Rep.*, **24**, 873–882.
64. Risca, V.I., Denny, S.K., Straight, A.F. and Greenleaf, W.J. (2017) Variable chromatin structure revealed by in situ spatially correlated DNA cleavage mapping. *Nature*, **541**, 237–241.
65. Cai, S., Chen, C., Tan, Z.Y., Huang, Y., Shi, J. and Gan, L. (2018) Cryo-ET reveals the macromolecular reorganization of *S. pombe* mitotic chromosomes in vivo. *Proc. Natl. Acad. Sci. U.S.A.*, **115**, 10977–10982.
66. Hihara, S., Pack, C.-G., Kaizu, K., Tani, T., Hanafusa, T., Nozaki, T., Takemoto, S., Yoshimi, T., Yokota, H., Imamoto, N. *et al.* (2012) Local nucleosome dynamics facilitate chromatin accessibility in living mammalian cells. *Cell Rep.*, **2**, 1645–1656.
67. Hansen, J.C., Connolly, M., McDonald, C.J., Pan, A., Pryamkova, A., Ray, K., Seidel, E., Tamura, S., Rogge, R. and Maeshima, K. (2017) The 10-nm chromatin fiber and its relationship to interphase chromosome organization. *Biochem. Soc. Trans.*, **5**, BST20170101.
68. Pepenella, S., Murphy, K.J. and Hayes, J.J. (2014) Intra- and inter-nucleosome interactions of the core histone tail domains in higher-order chromatin structure. *Chromosoma*, **123**, 3–13.
69. Zhu, P. and Li, G. (2016) Higher-order structure of the 30-nm chromatin fiber revealed by cryo-EM. *IUBMB Life*, **68**, 873–878.
70. Schubert, T., Pusch, M.C., Diermeier, S., Benes, V., Kremmer, E., Imhof, A. and Längst, G. (2012) Df31 protein and snoRNAs maintain accessible higher-order structures of chromatin. *Mol. Cell*, **48**, 434–444.
71. Maeshima, K., Kaizu, K., Tamura, S., Nozaki, T., Kokubo, T. and Takahashi, K. (2015) The physical size of transcription factors is key to transcriptional regulation in chromatin domains. *J. Phys. Condens. Matter*, **27**, 1–10.
72. Hughes, A.L. and Rando, O.J. (2014) Mechanisms underlying nucleosome positioning in vivo. *Annu. Rev. Biophys.*, **43**, 41–63.
73. Chereji, R.V., Ocampo, J. and Clark, D.J. (2017) MNase-Sensitive Complexes in Yeast: Nucleosomes and Non-histone Barriers. *Mol. Cell*, **65**, 565–577.
74. Voong, L.N., Xi, L., Wang, J.-P. and Wang, X. (2017) Genome-wide mapping of the nucleosome landscape by micrococcal nuclease and chemical mapping. *Trends Genet.*, **33**, 495–507.
75. Zlatanova, J. and Thakar, A. (2008) H2A.Z: view from the top. *Structure*, **16**, 166–179.
76. Bruce, K., Myers, F.A., Mantouvalou, E., Lefevre, P., Greaves, I., Bonifer, C., Tremethick, D.J., Thorne, A.W. and Crane-Robinson, C. (2005) The replacement histone H2A.Z in a hyperacetylated form is a feature of active genes in the chicken. *Nucleic Acids Res.*, **33**, 5633–5639.
77. Ausio, J. and van Holde, K.E. (1986) Histone hyperacetylation: its effects on nucleosome conformation and stability. *Biochemistry*, **25**, 1421–1428.
78. Poirier, M.G., Bussiek, M., Langowski, J. and Widom, J. (2008) Spontaneous access to DNA target sites in folded chromatin fibers. *J. Mol. Biol.*, **379**, 772–786.
79. Prior, C.P., Cantor, C.R., Johnson, E.M., Littau, V.C. and Allfrey, V.G. (1983) Reversible changes in nucleosome structure and histone H3 accessibility in transcriptionally active and inactive states of rDNA chromatin. *Cell*, **34**, 1033–1042.
80. Chen, K., Chen, Z., Wu, D., Zhang, L., Lin, X., Su, J., Rodriguez, B., Xi, Y., Xia, Z., Chen, X. *et al.* (2015) Broad H3K4me3 is associated with increased transcription elongation and enhancer activity at tumor-suppressor genes. *Nat. Genet.*, **47**, 1149–1157.